5
Results and discussion

5.1.
Biosurfactant extraction

Lang and Philp 1998 reported that surfactants produced by bacteria of the genre *Rhodococci* under unrestricted growth conditions are predominantly cell-associated trehalolipids therefore the broth was removed with the assumption that mostly of the biosurfactant was linked to the cell wall or contained inside the cell itself. In addition, previous bioflotation studies using *Rhodococcus opacus* reported the removing of the broth before the use of the biomass (Merma *et al.*, 2013). Based on the growth studies of Botero *et al.,* (2007) the *R. opacus* stationary phase starts after 24 hours since inoculation, where the curve levels off because the rate of cell inhibition or death balances out the rate of multiplication (Talaro *et al.*, 2015).

Regarding to the broth composition, although several works reported an increase in the biosurfactant production with the addition of long chain alkanes (>C10) as substrate (Tuleva *et al.,* 2008; Lang and Philp 1998; Tokumoto *et al.,* 2009). In order to make a reliable comparison of its potential as a biocollector against the bacteria itself, the broth culture was replicated from previous bioflotation studies using *Rhocococcus opacus* (Botero *et al.,* 2007, Botero *et al.,*2008, Merma *et al.,* 2013 and Mesquita *et al.,* 2003).

The crude biosurfactant recovery was 0.3 g/L of broth. Tuleva *et al.,* 2008 reported a recovery of 3.10 g/L in the presence of hexadecane. Due to the lower selectivity of ethanol towards triglycerides, during the extraction process other compounds such as phosphatides, polyphenols, pigments and soluble sugars are extracted jointly (Sineiro *et al.,* 1996). Regarding the temperature, Baümler *et al.,* 2015 reported a positive effect on the extractability of sunflower using ethanol. In addition, pressure reduces the solvent surface tension, which facilitates the penetration of solvent into the matrix pores, resulting in matrix disruption and

therefore enhances the mass transfer (Mustafa *et al.,* 2012). The final product, which is used in the flotation tests, was a solution containing the crude biosurfactant at an average concentration of 6200 ppm, the concentration was determined by weight measurements before and after resuspension in deionized water.

5.2. FTIR characterization of *Rhodococcus opacus* and the biosurfactant

Table 5-1 shows the possible functional found in the *Rhodococcus opacus* spectra. In the fingerprint region, below 1500 cm^{-1}, a large number of absorptions due to a variety of C-C, C-O and C-N single-bond vibrations may be occur; this region is unique for every substance (McCurry 2012). Additionally, it was found an intense peak between 1750 and 1620 cm^{-1} characteristic of aromatics, aldehydes, ketones and esters; Sharma 2001 reported the same peak. The mycolates that form part of the cell envelope and are responsible of the bacteria hydrophobicity (Sutcliffe *et al.,* 1998) may be reflected by the alkane, ketone and aldehyde peaks identified in the spectra. The presence of amino groups and aromatic compounds may be part of aromatic amino acids derived from proteic substances (Talaro *et al.,* 2015), which were reported to play a determinant role in flocculation and flotation processes (Patra *et al.,* 2008). Finally, the resonance at 1237.15 cm^{-1} may correspond to a phosphate group (Pohle at al., 2000), which could be part of the cellular membrane or nucleic acids.

Table 5-1: Possible functional groups identified by the FTIR spectra of *Rhodococcus opacus*

Wavenumber(cm-1)	Intensity	Possible functional group	Structures
3433.11	High	Alcohols	
3350.00	Medium	Amines	
2924.00	Medium	Alkanes	
1746.00	Medium	Aromatic, aldehydes, ketones, esters	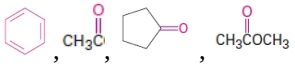
1632.00	High	Alkenes	
1548.59	Medium	Aromatic	
1400.78	Medium	Aromatic	
1237.15	Medium	Alkanes	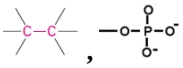
1079.02	Medium	Alkanes	

Regarding the crude biosurfactant, table 5-2 shows the possible functional found in the crude biosurfactant. The alkane, alkene, alcohol and ketone groups may indicate the presence of mycolic acids, which are produced by the *Rhodococci* typically with 28–54 carbons in total (Nishiuchi *et al.*, 2000). The identification of aromatic groups as well as amine groups could indicate the presence of polar amino acids such as tyrosine (Berg *et al.*, 2012).

Table 5-2: Possible functional groups identified by the FTIR spectra of the crude biosurfactant

Wavenumber(cm-1)	Intensity	Possible functional group	Structures
3397.94	High	Alcohols	
3350.00	Medium	Amines	
2929.27	Medium	Alkanes	
1629.44	High	Alkenes, ketones	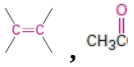
1400.41	Medium	Aromatic	
1047.35	Medium	Alkanes	

Finally, the similarity between both spectra as it is shown in Fig. 5-1 indicate that the biosurfactant was contained in the biomass, which also was used in microflotation tests.

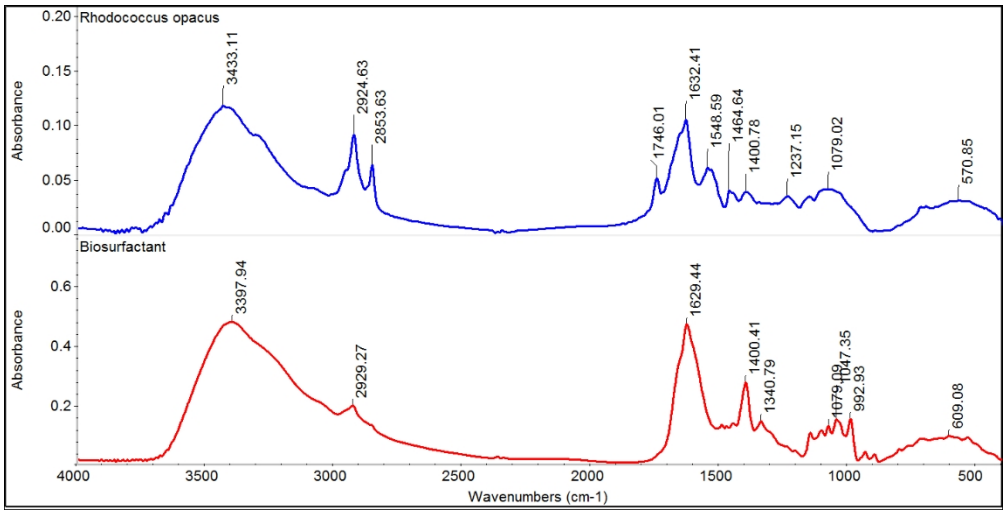

Figure 5-1: FTIR spectra of the crude biosurfactant (bellow) and Rhodococcus opacus (above).

Although, it was reported that bacterial proteins play a determinant role in flocculation and flotation processes because of its amphiphilic character (Patra 2008); in the case of using *Rhodococcus opacus* as bioreagent proteins may not be

the active substances responsible of conferring mineral hydrophobicity, because they would be denaturized by the inactivation process. However, the possible presence of amino and aromatic compounds may indicate soluble amino acids contained in the crude biosurfactant solution.

5.3. Hematite characterization

5.3.1. Fluorescence spectroscopy and EDS characterization

The mineral composition of the sample was determined throughout fluorescence spectroscopy. Table 5-3 shows the results, the sample is composed mostly of Fe_2O_3 with a percentage of 96.55%. The size fraction used in the test was +20 -38 µm.

Table 5-3: Fluorescence spectroscopy of hematite (+20 -38 µm).

Compound	%
Al_2O_3	0.0950
SiO_2	0.7700
P_2O_5	0.0350
SO_3	0.0700
CaO	0.0150
TiO_2	0.9350
V_2O_5	0.1000
Cr_2O_3	0.2215
MnO	-
Fe_2O_3	96.5500
CuO	0.0700
MgO	0.0650

In addition, elemental analysis was carried out by energy-dispersive X-ray spectroscopy (EDS). Evidently, the highest proportion was the iron. Table 5-4 shows the results.

Table 5-4: Hematite sample EDS

Element	Weight %	Atomic %
Oxygen	5.38	16.47
Aluminum	0.56	1.02
Iron	94.05	82.50
Total	100.00	100.00

5.3.2.
FTIR characterization of hematite

Fig. 5-2 shows the absorbance FTIR spectra of the hematite dry it at 50 °C for 24 h. The peaks at 463 and 540 cm^{-1} correspond to the vibration of the FeO bond (Haile *et al.*, 2015). In addition, hematite complexation may occur as a result of the interface mineral-water (Ma, 2012).

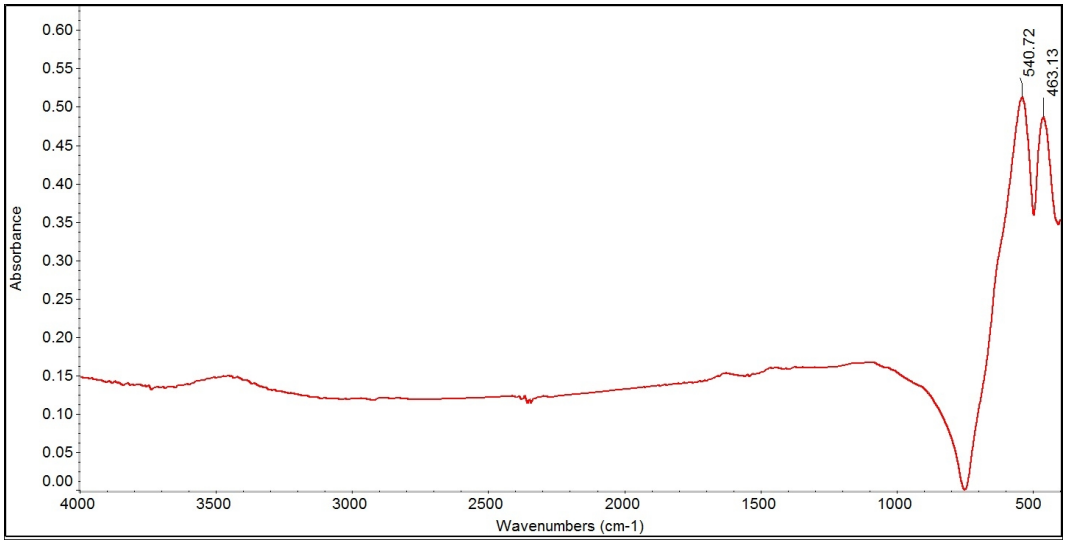

Figure 5-2: FTIR spectra of hematite.

5.4.
Electrophoretic studies

5.4.1.
Zeta potential measurements before crude BS adhesion

Fig. 5-3 shows the zeta potential of hematite particles varying the pH at three different background electrolyte concentrations. The background electrolyte concentration was varied in order to determine the point of zero charge, which is

independent of the indifferent ion adsorption (Myers 1999). In addition, there is a trend between the background electrolyte concentration and the zeta potential. Because of the electric double layer compression (Hiemenz *et al.*, 1997), the absolute value of the zeta potential at any pH decreases as the NaCl concentration rises. The IEP (isoelectric point) of hematite, with a background electrolyte concentration of 10^{-3} M, was around pH 7.5 and the PZC (point of zero charge) of hematite was around pH 7.6. Mesquita *et al.*, 2003 reported a hematite IEP of 5.1. For practical reasons, when no other ions except the potential determining ions and indifferent ions are present, the PZC and IEP can be approximated; however, they can differ in the presence of surface active ions, which are adsorbed in the Stern plane (Leja and Ramachandra 2004).

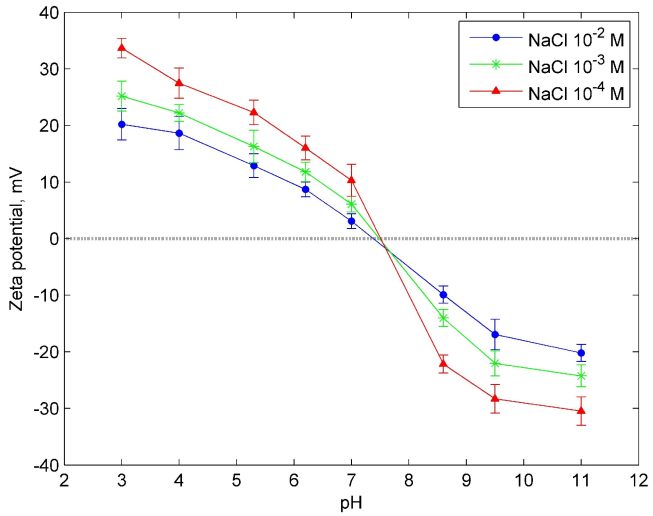

Figure 5-3: Zeta potential of hematite particles in function of the pH, size fraction -35 um, mineral concentration 0.1 g dm^{-3}, background electrolyte NaCl.

In order to explain the mechanism by which the hematite surface become positively or negatively charged depending on the pH; it is introduced the concept of surface groups by a general hydrolyzed species, ≡XOH. The surface complexation models of metal oxides assume that the surface contains one type of reactive surface group that can undergo two protonating steps (Gunnarsun 2002). Equation 5.1 and 5.2 shows the proposed model for the hematite complexation.

$$\rfloor FeOH_2^{\Gamma} \lfloor \quad \rfloor FeOH\Gamma H^{\Gamma} \tag{5.1}$$

$$\rfloor FeOH \lfloor \quad \rfloor FeO^{Z}\Gamma H^{\Gamma} \tag{5.2}$$

Therefore, at a pH lesser than 7.6, which is the PZC of hematite, there may be a prevalence of $\rfloor FeOH_2^{\Gamma}$ species, conferring its positive electric charge to the hematite surface. Near the PZC, there may be a predominance of the neutral specie $\rfloor FeOH$ and finally at pH values greater than the PZC the specie responsible for the negative electric surface charge may be the $\rfloor FeO^{Z}$.

5.4.2. Modelling of the diffuse layer

The electric double layer distribution was based on the Gouy–Chapman model or the diffuse double layer model and it was not considered specific adsorption (Myers 1999). This assumption is valid because the system is only composed of indifferent ions (Na^+ and Cl^-) and potential determining ions (H^+). If this criterion is obeyed, the diffuse layer theory can be applied (Hunter *et al.*, 2004).

The surface potential can be estimated applying the Nerst equation (Eq. 5.3). Where R is the gas universal constant , T is absolute temperature, F is Faraday constant, c is concentration of determining ions and c_{zp} is concentration of determining ions at the PZC. Furthermore, the equation is simplified for pure water at 25°C to the rightmost expression, where the potential is in mV (Hiemenz *et al.*, 1997).

$$\cdot_0 \mathrm{X}2.303\frac{RT}{F}\log\ \frac{c}{c_{zp}}\ \mathrm{X}59.17 fpH_{PZC}\ \mathrm{Z}\ pH \quad (5.3)$$

Throughout the Poisson–Boltzmann equation is possible estimate the potential distribution. However due to the complexity of the differential equation, the estimation is done with the assumption of a planar surface. The solution is an exponential function where the ratio between the potential and the distance from de surface is proportional to the potential itself. Equation 5.4 and 5.5 shows the differential equation and its solution for planar surfaces and low potentials (Butt *et al.*, 2003). Where ^{2} is the laplacian operator, $\cdot$ is the electric potential, which is function of the rectangular coordinates x,y and z; $\cdot_0$ is the surface potential; $°_e$ is the electrical density, ε is the water permeability and λ is the Debye lenght.

$$^{2}\cdot\ \mathrm{X}\frac{\left|^{2}\cdot\right.}{\left|x^{2}\right.}\Gamma\frac{\left|^{2}\cdot\right.}{\left|y^{2}\right.}\Gamma\frac{\left|^{2}\cdot\right.}{\left|z^{2}\right.}\mathrm{XZ}\frac{^{\circ}{}_{e}}{\pounds\pounds_{0}} \tag{5.4}$$

$$\cdot\ \mathrm{X}\cdot{}_{0}\exp\ \mathrm{Z}\frac{x}{\mathrm{a}_{D}} \tag{5.5}$$

The Debye length is defined as the inverse of the exponential decay constant κ; it is the distance at which the potential is reduced to 37% of the surface potential Equation 5.6 show the decay constant and the Debye length, in Å (10^{-10} meters), for water at 25°C and for a monovalent salt (Butt *et al.*,2003). Where c_0 is the NaCl concentration in mol-dm^{-3}, ε is the water permeability, k_B is the Boltzman contant and T is the absolute temperature.

$$\copyright\ \mathrm{X}\sqrt{\frac{2c_{0}e^{2}}{\pounds\pounds_{0}k_{B}T}}\ \mathrm{X}\frac{1}{\mathrm{a}_{D}} \tag{5.6}$$

Table 5-5 shows the estimated Debye length for the three background electrolyte concentrations. The Debye length decreases as the background electrolyte rises as consequence of the electric double layer compression (Hiemenz *et al.,* 1997). Manciu *et al.,* 2004 estimated the same compression applying the polarization model, which takes into account the additional interactions between ions and surfaces, not included in the mean field electrical potential.

Table 5-5: Debye length of hematite particles at three NaCl concentrations, particle size -35 um.

C_0 mol-dm^{-3}	Debye length Å
10^{-2}	30.40
10^{-3}	96.13
10^{-4}	304.00

Applying the equation 5.6, substituting the Debye length and the surface potential, which is dependent of the pH, it is obtained the electrostatic potential distribution. The results, at different pH, are shown in Fig. 5-4. Note how near the IEP the slope of the curve decreases as result of the potential decrease. In addition, the interaction distance of the electric layer decreases as the pH approaches the

PZC, this is consequence of the electric double layer compression Hunter et al. (2004).

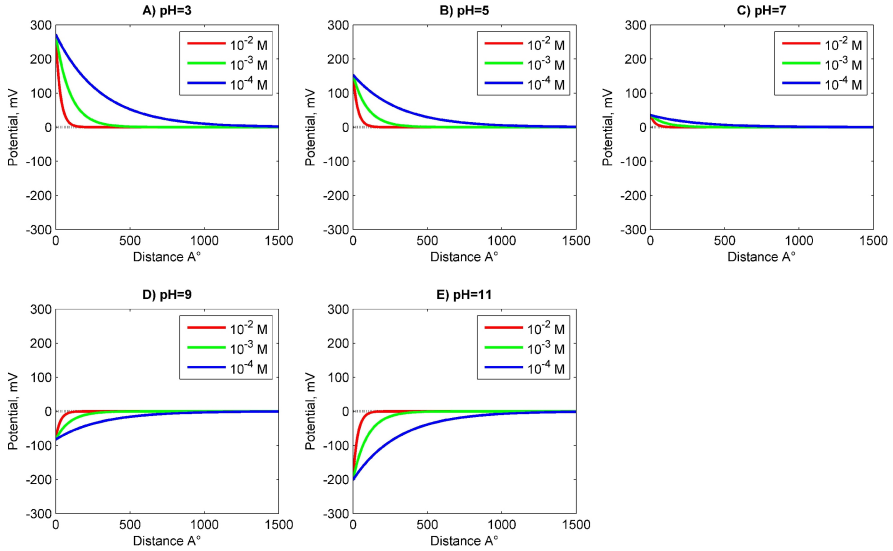

Figure 5-4: Potential distribution applying the diffuse layer model for hematite particles of -35 µm, background electrolyte NaCl at pH 3(A), pH 5(B), pH 7(C), pH 9(D) and pH 11 (E).

As was mentioned before, the solution of the Poison Boltzman equation for a sphere is complex. In fact, there is no analytical solution and numerical methods must be applied (Butt *et al.*, 2003). However, it is possible to visualize how the potential vary around a spherical particle by rotating the potential distribution function around the vertical axis, such parameterization technique can be found in Steward et al. (2012). The final equations are Eq. 5.7, Eq. 5.8 and Eq 5.9, where the parameter *t* is the distance in A°, x, y and z are the rectangular coordinates and θ is the rotation angle (from 0 to 360°).

$$z = X \cdot_0 \exp\left(Z \frac{t}{a_D}\right) \tag{5.7}$$

$$x = Xt\cos^{-} \tag{5.8}$$

$$y = Xt\sin^{-} \tag{5.9}$$

Fig. 5-5 shows the potential distribution for a spherical particle, applying the equation above, for an ultrafine particle of 0.1 μm. The Z-axis represents the electrostatic potential, and the XY-plane the special coordinates. The color bars at the right of the plots, indicate the potential magnitude. The potential is higher at the extreme pH values and decreases until zero when it reaches the PZC, therefore the

electrostatic interaction of the particle is going to be greater very acid and basic pH, similar behavior was reported by Mesquita *et al.*, 2003.

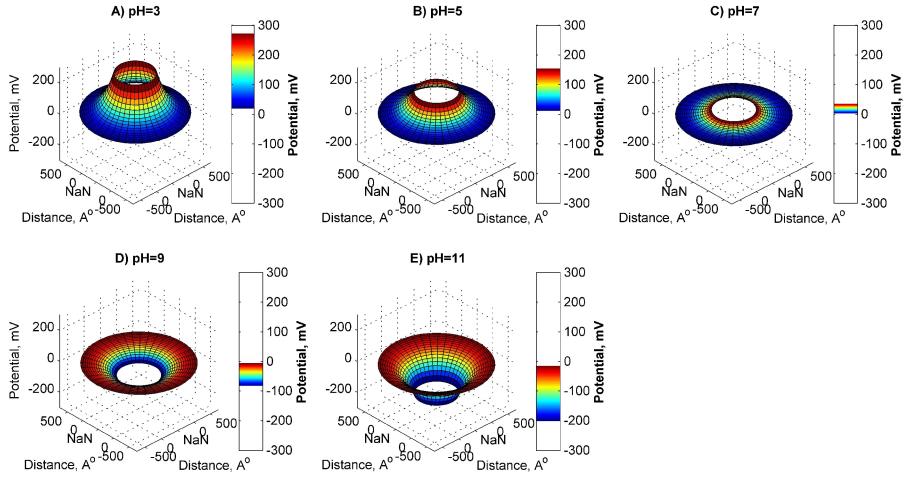

Figure 5-5: Potential distribution of a spherical particle applying the diffuse layer model, at pH 3(A), pH 5(B), pH 7(C), pH 9(D) and pH 11 (E), background electrolyte NaCl 10^{-3} M.

Fig. 5-6 shows the electrostatic potential map of hematite in function of the distance and pH for the three background electrolyte concentrations. Every isoline represents a constant electric potential. The dense areas indicate a greater electric potential, they were found at the extremes of the pH range between 3 and 11, and near the mineral surface, as the Boltzman-Poison equation describes. In addition, near the isoelectric point, around pH 7.6, it can be seen a less dense area with isolines corresponding values near zero for the three electrolyte concentrations. The fact that this less dense zone does not vary and it is the same for the three graphs supports the idea that the PZC is not affected by Na^+ or Cl^- ions, which are known as indifferent ions (Myers 1999). Note how the interaction distance of the electric double layer decreases as the electrolyte concentration rises as consequence of the electric compression (Hiemenz *et al.*, 1997).

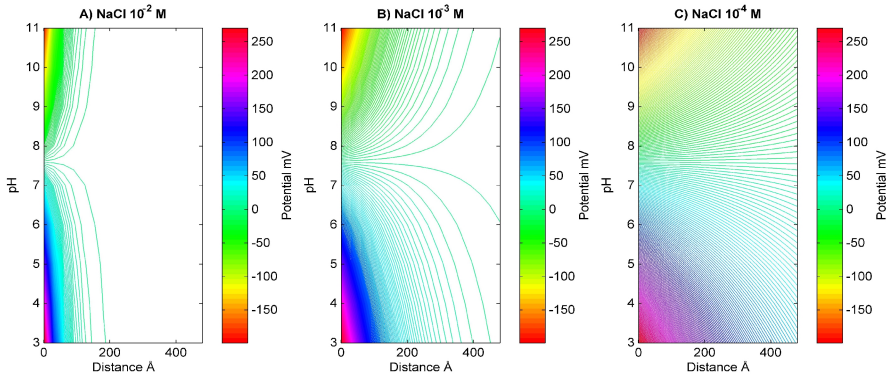

Figure 5-6: Electrostatic potential map as function of the distance and pH at three background electrolyte concentrations of NaCl for hematite particles of size fraction -35 µm.

5.4.3.
Zeta potential measurements after crude BS adhesion

Fig. 5-7 shows the effect of the crude biosurfactant on the zeta potential of hematite at a background electrolyte of 10^{-3} M. The characteristic IEP shift toward the acidic region was reported also in several bioflotation studies using the bacteria *Rhodococcus opacus* (Botero *et al.*, 2007; Mesquita *et al.*, 2003; Merma *et al.*, 2013).

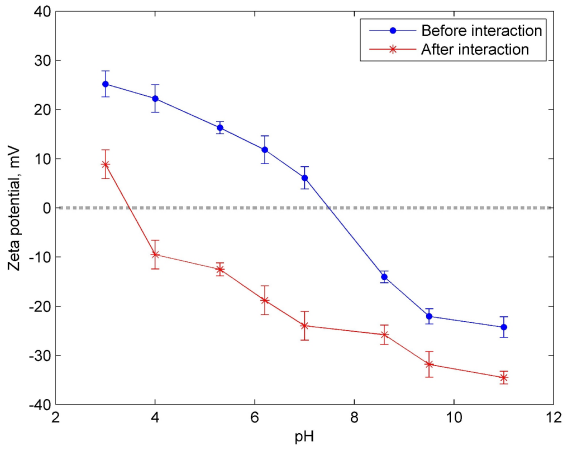

Figure 5-7: Zeta potential of hematite particles before and after interaction with the crude biosurfactant, size fraction -35um, mineral concentration 100 ppm, NaCl 10 -3 M, BS concentration 120 ppm.

Fuerstenau et al. (2005) reported a similar behavior of hematite particles treated with oleate, however there was no evidence of oleate adsorption onto the hematite surface at pH values greater then 9, because the zeta potential was not affected. This was supported by the fact that oleate is an anionic collector, therefore exist electrostatic repulsion at pH values greater than the hematite IEP. On the other

hand, it can be seen that the zeta potential profile of the hematite sample after interaction with the BS is altered even at basic pH values. The trehalolipids, linked to the *Rhodococcus opacus* cellular wall, can be presented in its non-ionic form as trehalose-dimycolates or in its anionic form as trehalose-tetraester, being the carboxyl group ionizable (Lang and Philp 1998).

It is worth to highlight that the crude biosurfactant is not only composed of trehalolipids. In fact, it is a mixture of different organic substances such as polysaccharides, fatty acids, phospholipids and even there may be soluble amino acids. Although the zeta potential profile indicates that there is adsorption of the crude biosurfactant in all the pH range studied, there may be different substances adsorbed depending on the pH. For instance, an anionic surfactant could be adsorbed in the pH band bellow the hematite IEP by electrostatic interactions, on the other hand a non-ionic substance or even a cationic group such as ($-NH3^{+}$) could be adsorbed on the remaining band. Therefore, alteration of the hematite surface does not guarantee the adsorption of solely amphiphilic substances. In addition, the significant IEP shift may indicate specific adsorption (Fuernesteau *et al.*, 2005) and therefore, the new IEP, which cannot be approximate to the PZC, reflects the hydrophobic chain of the surfactant displacing water molecules from the particle surface.

5.4.4. Combined approach of the plate capacitor and the Guoy-Chapman model

The adsorption of the biosurfactant onto the mineral surface can be modelled with the following restrictions: (1) The charge density on the mineral surface remains constant under all conditions; (2) discarding the effect of “charge regulation” which dictates that as two charged surfaces are brought together, the surface charge density becomes a function of the distance of separation and tends toward zero at contact (Myers 1999) and (3) the crude biosurfactant is specifically adsorbed, which is supported by the significant IEP shift presented in the modified hematite.

In this case, the system is composed of potential determining ions, indifferent ions and specific adsorbed ions; therefore, it cannot be adapted to the diffuse model of Gouy–Chapman. The proposed solution is to divide the distribution in two areas, the first area in which the ions are specifically adsorbed can be modelled as a plate capacitor where the potential decreases linearly (Myers 1999); the second area obeys the Gouy–Chapman model where the potential decreases exponentially. Equation 5.10 shows the plate capacitor model (Hiemenz *et al.*, 1997), where ψ is the electrostatic potential (mV), δ is the distance from the mineral surface to the shear plane (A°), σ is the charge density (C/m^2), ε_r is the dielectric constant of water (its bulk value around 80) and ε_0 is the vacuum permittivity ($8.85*10^{-12}$ $C^2J^{-1}.m^{-1}$).

$$\frac{d\cdot}{dx} = \frac{\zeta\cdot}{\text{¢}} = \frac{\pm}{\text{£}_r\text{£}_0} \tag{5.10}$$

In order to estimate the distance between the mineral surface and the new shear plane, formed because of the specific adsorbed ions, it is required to know the charge density, which can be estimated applying the Grahame equation (Butt 2003). Equation 5.11 and 5.12 shows its differential form and its simplified solution for low potentials. The dielectric constant of water at a NaCl concentration of 10^{-3} M can be approximated to that of pure water with no significant error (Gavish *et al.*, 2012).

$$\pm = \text{£}_r\text{£}_0 \int_0^{|} \frac{d^2\cdot}{dx^2} dx \tag{5.11}$$

$$\pm = \frac{\text{£}_r\text{£}_0\cdot_0}{\text{a}_D} \tag{5.12}$$

Fig. 5-8 shows the estimated charge density in function of the pH and the shear plane distance before and after interaction with the crude biosurfactant. The charge density is linearly affected by the pH, however Trefalt *et al.*, 2015 reported a non-linear trend of charge density obtained by potentiometric titration. The difference may be attributed to the constraint of charge regulation absence. The shear plane distance of hematite at the PZC was marked as zero because there is no

electric layer formation at that point (Hiemenz *et al.*, 1997). Note how the distance decreases as the pH approaches the PZC and following it rises, before biosurfactant interaction. The electric potential at the extreme pH is greater than at the center, therefore at the extremes the particle may be capable of attract more water dipoles developing a thicker Stern layer. This is supported by the variation of the water dielectric constant near iron ore interfaces (Ma 2012). Regarding the modified hematite it seems there is a break in the trend at between pH 7 and 8; this may be the result of the electrostatic repulsion between the biosurfactant and the negatively charged hematite above the PZC and the adhesion of non amphiphilic substances that may affect negatively the mineral floatability (Shibata *et al.*, 2003).

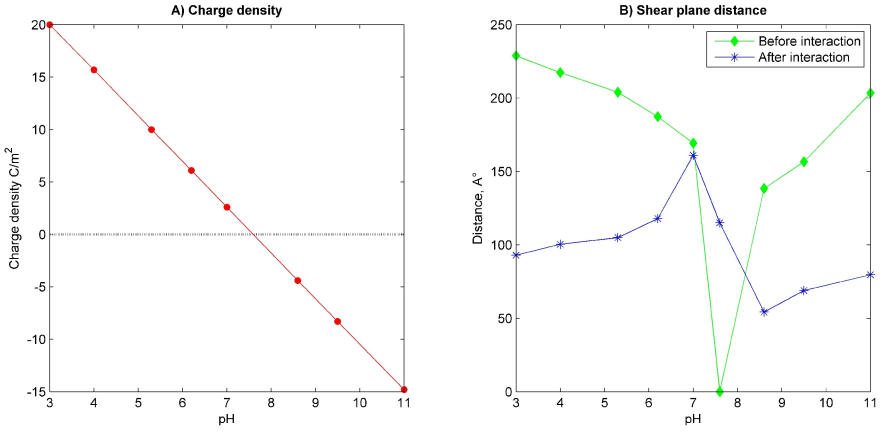

Figure 5-8: Estimated charge density of hematite particles as function of the pH applying the Grahame equation simplified for low potentials (A), Shear plane distance before and after biosurfactant interaction (B).

Fig. 5-9 shows the hematite potential distribution before and after interaction with the crude biosurfactant. The electric potential drops linearly until it reaches the new shear plane, based on the capacitor model. After the shear plane, the potential drop can be described by the Guoy-Chapman model (Myers 1999). At pH 3 and 5, the potential drop of the modified hematite is significant, decreasing the interaction distance of the electric double layer. This may facilitate the attachment of the particles to hydrophobic phases such as air. At pH 7, the reversal charge is more evident and the zeta potential of the modified hematite becomes more negative as the pH is incremented. Therefore, at a pH greater than 7 the particles become more charged which may hinder their adhesion to hydrophobic surfaces. Vilinska and Rao (2008) proposed that the zeta potential drop of the

mineral after interaction with the bioreagent was due to adsorption of the cells and/or metabolic products onto the mineral surface.

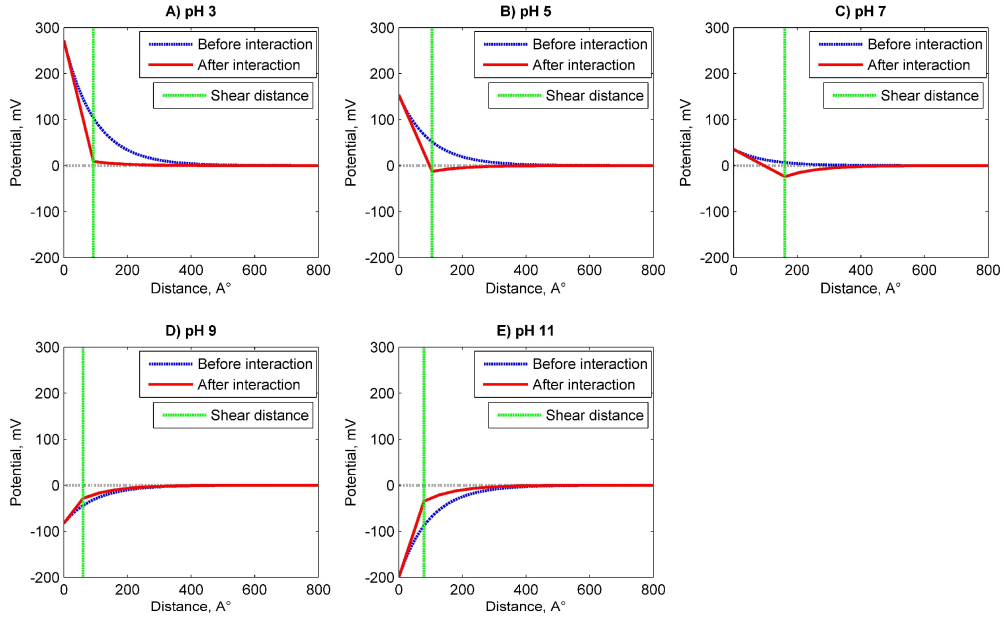

Figure 5-9: Potential distribution before and after crude BS adsorption, applying the mixed model; background electrolyte NaCl 10 $^{-3}$ M, particle size -35 µm.

5.4.5. Thermodynamic demonstration of the electric double layer formation of hematite particles

It also possible to demonstrate thermodynamically the spontaneous formation of the electric double layer. Summing up all contributions, the total Gibbs free energy of the diffuse double layer per unit area is shown in Eq. 5.13 and its simplified form for low potentials in Eq. 5.14 (Butt *et al.*,2003). Where ΔG is the Gibbs free energy per unit area, σ is the electric density, ψ_0 is the surface potential, κ is the exponential constant defined as the inverse of the Debye length, ψ_0' is the surface potential at a determinate moment.

$$\zeta G \, \mathrm{XZ} \pm \cdot {}_0\Gamma^{\pm}_{0} \cdot {}'_0 d \pm {}' \tag{5.13}$$

$$\zeta G \, \mathrm{XZ} \frac{\copyright £ £_0}{2} \cdot {}^{2}_{0} \tag{5.14}$$

Fig. 5-10 shows the variation of Gibbs free energy as a function of the pH, at 25°C and assuming pure water. It can be seen that at acid pH 3 the double layer formation is more energetically favorable than at basic pH 11. This is in agreement with the shear plane distance estimation showed in Fig. 5-9, where at pH 3 the layer was thicker than at basic pH 11. Finally, as the pH approaches the PZC, the stability of the electric double layer decreases. When it reaches the PZC the net free energy is zero which indicate no formation of the electric double layer (Vainrub *et al.*, 2000).

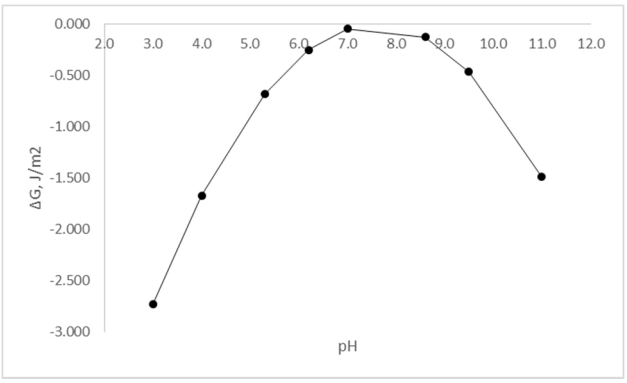

Figure 5-10: Gibbs free energy variation of the electric double layer in function of the pH for hematite particles of -35 µm and NaCl (10^{-3} M) as background electrolyte.

5.5. Surface tension measurements

Fig. 5-11 shows the surface tension of deionized water in function of the crude biosurfactant concentration at neutral pH. The estimated CMC is around 92 ppm and the surface tension decreases until 50.5 mN/m. Most of the biosurfactants found in the *Rhodococcus* genus were reported to low the surface tension of water from 72 mN m^{-1} to values between 19 and 43 at CMC between 17 and 37 ppm after refination processes (Christova *et al.*, 2014).

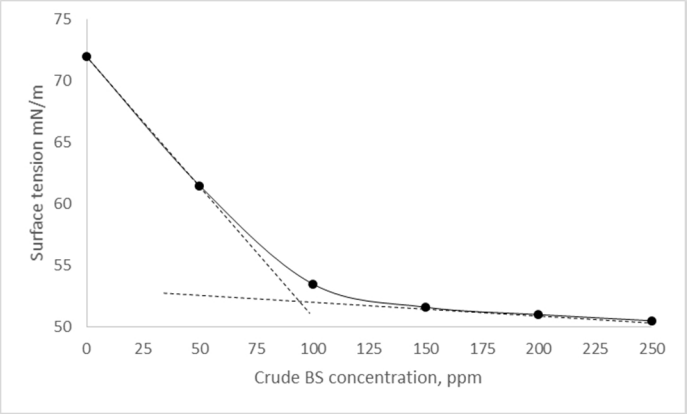

Figure 5-11: Effect of the crude biosurfactant concentration on the surface tension of water at 23°C and pH 7.

5.6. FTIR analysis of the modified hematite

Fig. 5-12 shows the FTIR spectra of the hematite before and after biosurfactant interaction at pH 3. The characteristic peaks of hematite, 540 and 433.13 cm^{-1}, are maintained. In addition, the new peak formed at 3456 cm^{-1}, may correspond to –OH vibrations. A similar peak was reported in the FTIR of magnesite and calcite after interaction with *Rhodococcus opacus* (Botero *et al.,* 2008). The peaks at 2923 cm^{-1} and 1631 cm^{-1} correspond to alkane and carboxyl vibrations respectively. Interestingly, there is no resonance for amino groups, which may indicate the absence amino acids onto the modified hematite surface. Although the FTIR spectra of the crude biosurfactant showed a wide range of functional groups such as amino, carboxyl, aldehydes, alkenes and alcohols; the spectra of the modified hematite show that not all the compounds get to the surface. Based on the electrophoretic studies, anionic species would have more probability of reach such surface, assuming the predominance of electrostatic interaction (Lyklema 2009). The FTIR spectra of the modified hematite at pH values of 3, 5, 7 and 9 can be found in the appendix D. Finally it is necessary to highlight, that the crude biosurfactant is in fact a mixture of unidentified substances, these peaks are not guarantee of the adsorption of amphiphilic substances onto the hematite surface.

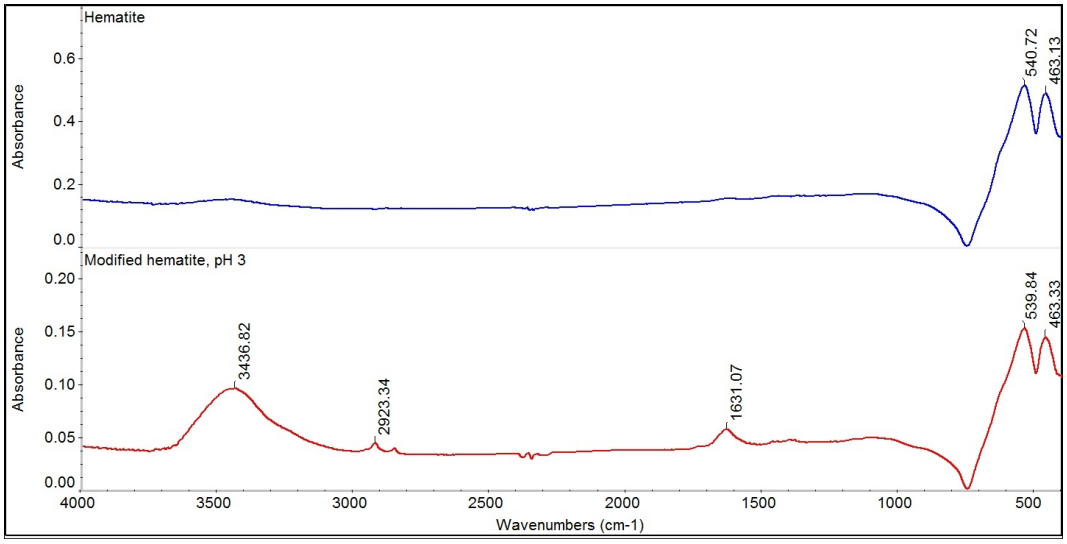

Figure 5-12: FTIR spectra of hematite particles (-35 µm) before and after interaction with the Rhodococcus opacus' crude biosurfactant.

5.7. Microflotation studies

5.7.1. Hematite flotation with *Rhodococcus opacus* as reagent

Fig. 5-13 shows the hematite recovery using *R. opacus* as bioreagent varying the pH and the concentration. An optimum hematite recovery of 43.5 % was reached at pH 7 with a concentration of 100 ppm. Zeta potential studies showed that the hematite and the bacteria have an IEP of 7.1 and 3.2 respectively (Mesquita *et al.*,2003). Therefore, at pH 3 should be electrostatic repulsion hindering the adhesion bacteria-hematite and consequently decreasing the hematite recovery in the flotation tests. At pH 5 the bacteria and mineral have opposed electric charges and therefore the adhesion mineral-bacteria should improve resulting in an increase in the hematite recovery. Finally, at pH 7 the hematite has little electrostatic interaction with other particles suggesting that Van Der Waals forces may predominate forming a hydrophobic cage around the hematite mineral (Pashley *et al.*, 2004).

The bacteria *Rhodococcus opacus* is covered with mycolic acids whose unsaturated chains are point perpendicularly to the exterior (Kuyukina *et al.*, 2010). Therefore, it is possible suggest a mechanism by which the hydrophobic bacteria can be attached to the mineral surface by non-electrostatic forces. This is supported

by the fact that at pH 7, the hematite particles are near its PZC and they present good floatability as the biomass concentration is incremented, which in turn, is a strong evidence of bacterial adhesion. In other words, at pH 7 the hematite does not repel the bacteria, resulting in a hydrophobic interaction, enclosing the hematite particles. Mesquita et al. (2003) reported high hematite floatability at pH between 5 and 7.

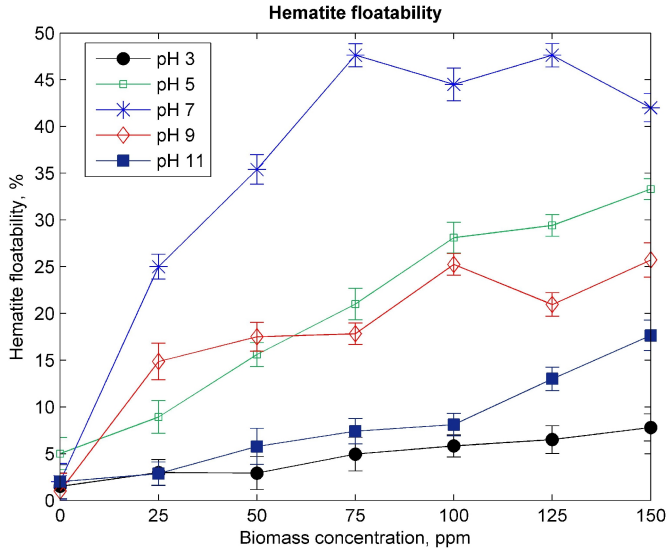

Figure 5-13: Hematite floatability in function of pH and biomass concentration, NaCl 10^{-3} M as background electrolyte, size fraction +75-150 µm, conditioning time 2.5 min, flotation time 2.5 min and air rate of 35 L/min.

Therefore, the adhesion of the modified mineral covered with the biomass or soluble substances, which were originally part of bacteria, can be explained by the mechanism shown in Fig. 5-14. The biomass charge acquisition could be the result of partial releasing of the mycolic acids from the bacterial surface as well as the lysis suffered by the cells during the inactivation phase, usually carried out by autoclaving. The remaining mycolic acids attached to the outer cellular wall may still have an important function in the flotation process, this is support by the fact that contact angles measurements showed that the modified hematite still presented relatively high angles in all the pH range (Merma *et al.*, 2013) and not only at the isoelectric point of *Rhodococcus opacus*. Therefore, it is proposed that the hydrophobic tail of the remaining mycolic acids attach to the air bubble and consequently the modified mineral is floated.

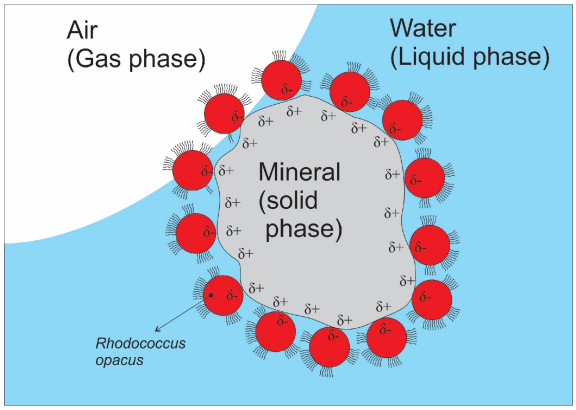

Figure 5-14: Proposed adhesion mechanism of Rhodococcus opacus with the mineral (solid phase) and the air (gas phase), the tails represent the hydrocarbonic chains of the mycolic acid that surrounds the cellular wall.

Fig. 5-15 shows the effect of the pH and the biomass concentration onto the hematite floatability, the red lines represent the mean values. at pH 7 the hematite floatability reaches its maximum, zeta potential measurements of the mineral (Fuerstenau *et al.*, 2005) showed that at neutral pH the hematite has little electrostatic interaction because the proximity of its PZC, therefore maximizing the adhesion of the hydrophobic bacteria. In addition, the biomass concentration has a positive effect until it reaches 100 ppm, thereafter the average is almost constant, this may be explain because the suspension approaches its critical micelle concentration (CMC).

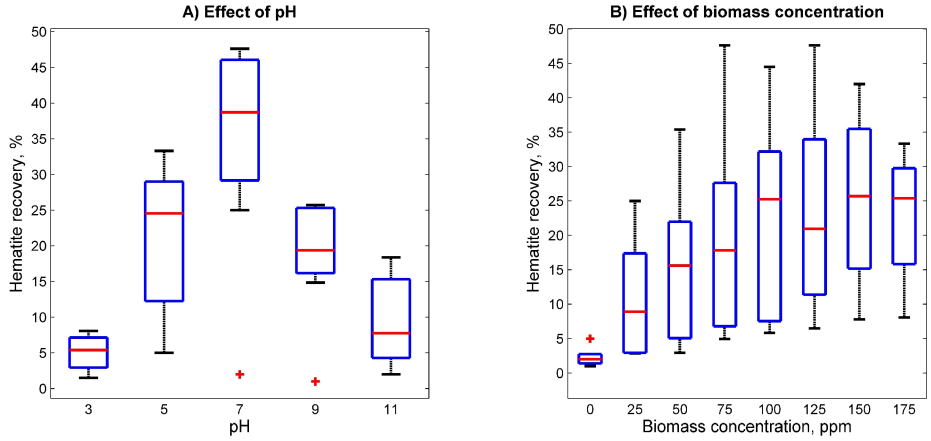

Figure 5-15: Variability of hematite floatability in function of the pH (A) and biomass concentration (B).

The effect of the biomass concentration and pH was analyzed based on the p-value criteria. The p-value can be interpreted as the probability that the variability of the response comes from the inherent randomness of the process (Walpole *et*

al., 2012). Table 5-6 shows the estimated coefficients of the statistical model, where x_1 is the pH and x_2 is the bacterial concentration, with their respective p-value. The terms x_2^2, x_2^3 and $x_1.x_2^2$ do not affect significantly the hematite recovery and can be discarded in the model.

Table 5-6: Coefficients of the polynomial regression with *Rhodococcus opacus* as reagent.

Coeficients	Estimate	p-value
Intercept	264.2485	6.32E-06
x_1	-188.1912	3.31E-06
x_2	-1.6911	4.99E-05
x_1^2	46.1947	2.03E-06
$x_1.x_2$	0.7419	2.31E-06
x_2^2	0.0077	0.0222
x_1^3	-4.6570	1.69E-06
$x_1^2.x_2$	-0.0697	0.0001
$x_1.x_2^2$	-0.0027	4.18E-05
x_2^3	-6.37E-06	0.5661
x_1^4	0.1651	1.77E-06
$x_1^3.x_2$	0.0016	0.0373
$x_1^2.x_2^2$	0.0002	1.50E-06
$x_1.x_2^3$	1.07E-06	0.466

The adjusted model was a polynomial function of 4th and 3rd order for the pH and biomass concentration respectively with a correlation coefficient (R^2) of 93.6%. Makhija et al. (2014) determined a second order model using oleic acid as collector of iron minerals. Polynomial models of lesser order where tried, such as 1-1, 1-2, 2-1, 2-2, 2-3 until 3-3 for the pH and biomass concentration respectivelly. However their correlation coefficients where lower than 60 %, and therefore they were discarded. Eq. 5.15 shows the empirical model.

$$R = p_{00} + p_{10}x_1 + p_{01}x_2 + p_{20}x_1^2 + p_{11}x_1x_2 + p_{30}x_1^3 + p_{21}x_1^2x_2 + p_{12}x_1x_2^2 + p_4x_2^4 + p_{31}x_1^3x_2 + p_2x_1^2x_2^2 \quad (5.15)$$

The surface response contrasted with the real data is presented in the Fig. 5-16 (A). The corresponding isolines of the polynomial function is presented in Fig, 5.16 (B). At the extremes of the pH range, the lines are blue indicating a low hematite floatability, less than 10% and they are not affected by the raise on the biomass concentration. On the other hand, at neutral concentration, it can be seen

how the isolines turn red as the biomass concentration increases; representing a hematite recovery between 40 and 45%. The optimum value was found at the eye of the contour plot, at pH 7 and biomass concentration of 125 ppm.

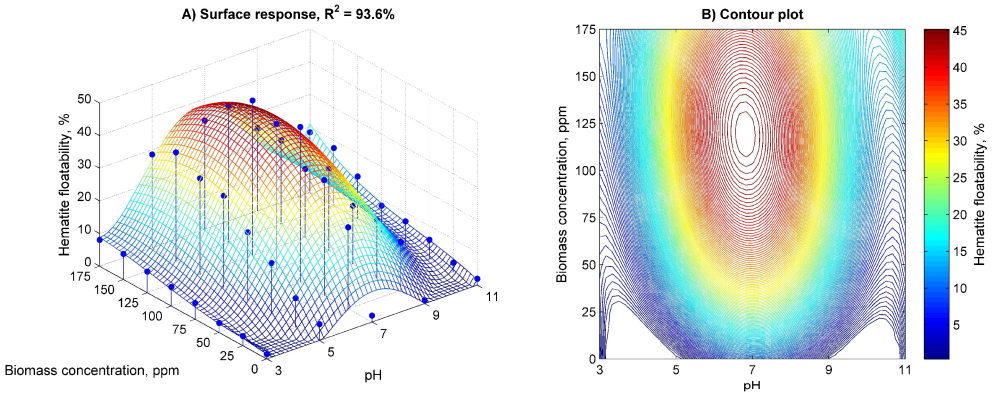

Figure 5-16: Surface response (A) and contour plot (B) of hematite floatability with the biomass.

5.7.2. Hematite flotation with the crude biosurfactant

Fig. 5-17 shows the hematite recovery using the crude biosurfactant extracted from the *Rhodococcus opacus* by hot ethanol. The most contrasting difference, regarding bioflotation with the bacteria, is that the optimum of hematite floatability is reached at pH 3, whereas in flotation tests with *Rhodococcus opacus* the hematite recovery was minimum at similar conditions. In addition, the hematite recovery is about 96%, whereas with the bacteria the maximum was 43.5 %.

Comparing with synthetic collectors, it seems that the BS has a similar behavior with the sodium dodecyl sulfate, which was reported to had a hematite recovery of 95 % at acid pH (Vidyadhar *et al.*, 2014). However, this is a rough comparison and in order to carry out valid contrasting between the BS and synthetic collectors, experimental conditions must be similar.

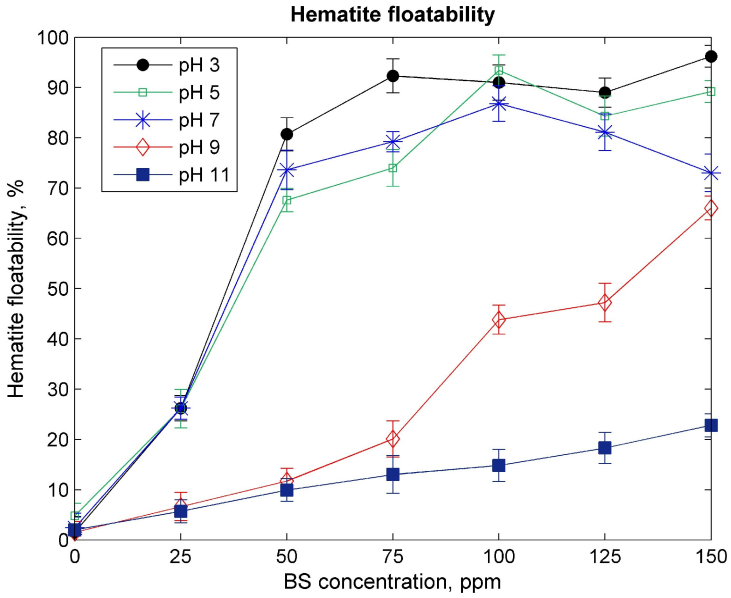

Figure 5-17: Hematite floatability in function of the pH and BS concentration, NaCl 10^{-3} M as background electrolyte, size fraction +75-150 µm, conditioning time 2 min, flotation time 1 min and air rate of 35 L/min.

Literature review suggest that most of the non-toxic biosurfactants are anionic (Christova *et al.*, 2014); in addition, based on electrophoretic studies, the hematite IEP was reported around 7.1. It is easy to see the correlation between the pH and the BS adhesion. At acid pH there is going to be electrostatic attraction between the mineral surface and the anionic BS, resulting in maximum adhesion and therefore maximum hematite recovery. On the other hand at basic pH there is going to be minimal adhesion because of the electrostatic repulsion. Another difference between the use of the bacteria and the BS in hematite flotation was the amount of froth produced. The BS produced a stable froth, even though in less amount comparing with the bacteria.

Fig. 5-18 shows the effects of pH and BS concentration onto hematite floatability. The pH affects negatively the hematite recovery, which could be explained by the electrostatic repulsion between the hematite surface and the hypothetical anionic surfactant. Additionally, the variability decreases as the pH is incremented. Regarding the effect of the concentration, at values greater than 100 ppm, the hematite floatability is stable, this is in agreement with the surface tension measurements where it was showed that the crude biosurfactant had a CMC around 100 ppm.

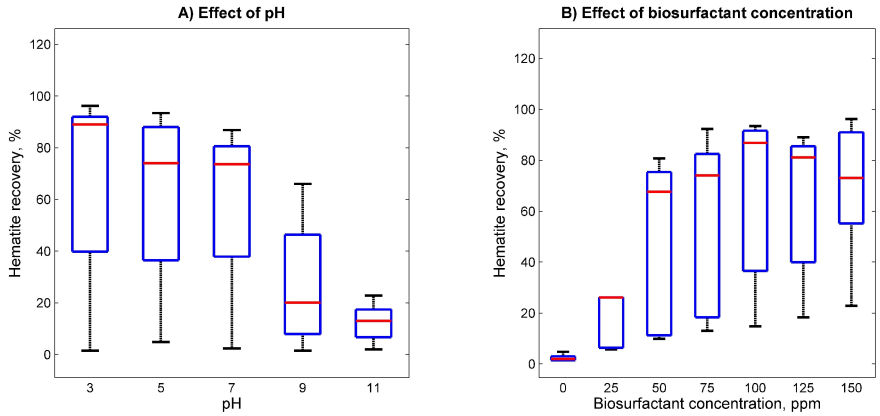

Figure 5-18: Variability of hematite floatability in function of the pH (A) and crude biosurfactant concentration (B).

Table 5-7 shows the coefficients for the polynomial regression of the hematite recovery in function of the pH, x_1, and BS concentration, x_2, with their respective p-values.

Table 5-7: Coefficients of the polynomial regression with the crude biosurfactant as reagent.

Coeficients	Estimate	p-value
Intercept	-11.14366	0.6277
x_1	3.56417	0.6099
x_2	2.31864	5.64E-05
x_1^2	-0.23980	0.6229
$x_1.x_2$	-0.09883	0.2697
x_2^2	-0.01343	0.0146
$x_1^2.x_2$	-0.00885	0.1099
$x_1.x_2^2$	0.00113	6.56E-04
x_2^3	0.00001	0.7380

The polynomial regression is of 2nd order on the pH and 3rd order on the BS concentration. Following the p-value criteria all the terms that have a p-value greater than 0.005 are discarded. It is interesting to highlight that qualitatively it seems that the pH has a significant effect onto the hematite recovery, however statistically is demonstrated that the real effect is a combination between the pH and the quadratic term of BS concentration.

Eq. 5.16 shows the polynomial function, where it was discarded the highlighted terms of Table 5-7 because their no-significance. The polynomial

regression using the biosurfactant against the bacteria is simpler. This may be an evidence of how the hematite flotation using the *Rhodococcus opacus*' biosurfactant is easily controlled contrasting the use of the bacteria itself.

$$R \mathrm{X} p_{01} x_2 \Gamma p_{12} x_1 x_2^{\ 2} \tag{5.16}$$

The surface response with the real data is shown in Fig. 5-19. The correlation coefficient of the polynomial regression was 91.1%. The red isolines represent a hematite floatability greater than 75%. The optimum region is between pH 3 and 7 and biosurfactant concentration greater than 75 ppm.

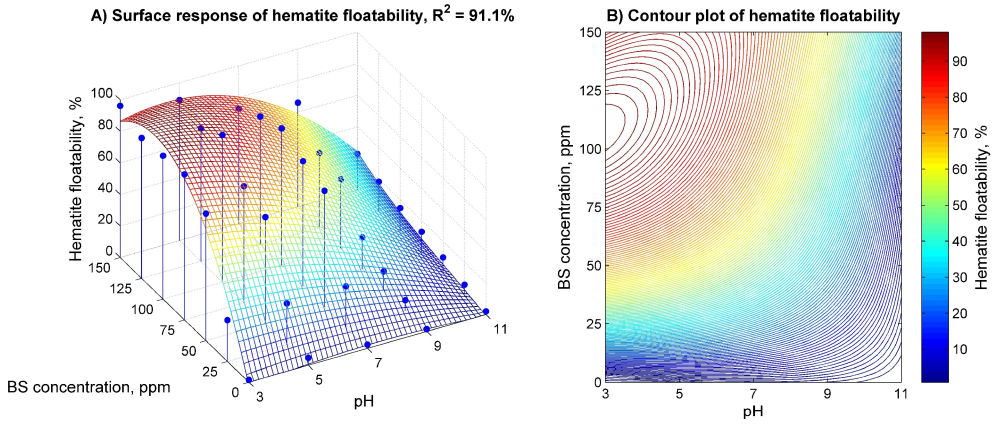

Figure 5-19: Surface response (A) and contour plot (B) of hematite floatability with the biosurfactant.

Fig. 5-20 shows a bar diagram comparing the hematite recoveries using the biosurfactant and the bacteria *Rhodococcus opacus*. In order to evaluate this contrasting, both experiments were conducted at similar conditions, airflow, conditioning time, flotation time, size fraction and background electrolyte concentration. The hematite floatability using the biosurfactant is greater at all the pH levels. While the maximum hematite recovery using the bacteria resulted at pH 7, the biosurfactant had an optimum at pH 3. Finally, the flotation time using the biosurfactant is lesser than using the bacteria as bioreagent.

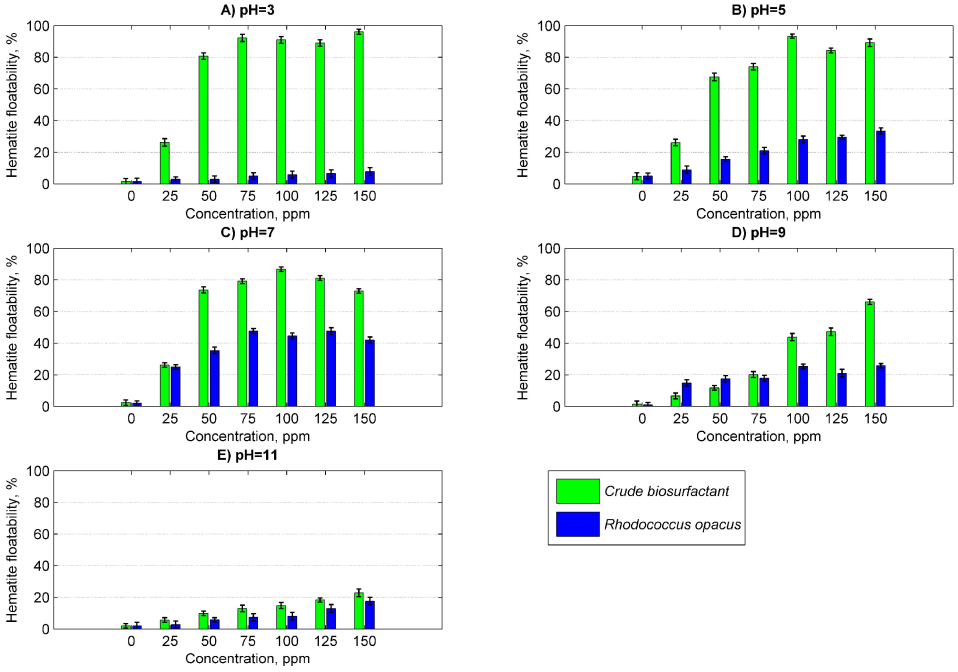

Figure 5-20: Bar diagram comparing hematite floatability using the crude biosurfactant (green) and the Rhodococcus opacus (blue).